COMMUNICATION

Electrophoretic deposition of supramolecular complexes for the formation of carbon nitride films

Liel Abisdris[a], Jonathan Tzadikov[a], Neeta Karjule[a], Adi Azoulay[a], Michael Volokh[a], Menny Shalom[*a]

The large-scale fabrication of polymeric carbon nitride (CN) films with tunable thickness, composition and photoelectrochemical properties is reported. To do so, we deposited supramolecular complexes as seeding layers prior to a thermal deposition of melamine vapor. The seeding layer is succesfuly formed by employing electrophoretic deposition of the supramolecular complexes on various substartes. The CN films exhibit good photoelectrochemical activity due to strong adhesion to the substrate, which allows a fast electron transfer and hole extraction to the electrolyte.

Polymeric carbon nitride (CN) has emerged as a promising material for various catalytic reactions, spanning photo-, electro- and organo-catalysis,[1-4] owing to its tunable band gap, suitable energy bands position, high stability to harsh chemical environment, easy preparation and low cost.[5, 6] However, while meaningful advances have already been achieved in CN chemistry and utilization as a powder,[7, 8] the exploitation of CN materials in (opto)electronic and photoelectrochemical devices such as photovoltaic cells, light-emitting diodes, and photoelectrochemical cells (PEC) is still at an early stage due to the challenge of depositing uniform and controlled CN layers on substrates.[9, 10] Moreover, for many devices, intimate contact with the substrate surface should be established to enable good electronic conductivity and strong adhesion in a solution.

Recently, several methods, which are based on the direct growth of CN film or by vapor deposition methods were successfully introduced.[11-14] Each method possesses several advantages such as controlled optical and chemical properties for the direct growth and substantial control over the homogeneity and thin layer formation for the vapor route. However, despite the achievable control of the vapor method, the surface wettability and chemical structure strongly affect the resulting layer quality and thickness. Moreover, vapor methods endow great control of the thickness up to several hundred nanometers, while for some applications, a much thicker layer is required.

Electrophoretic deposition (EPD) is considered as an easy, scalable and benign method to deposit various nano- and micro-scale objects ranging from ceramics,[15, 16] through carbon nanostructures,[17, 18] to metal and semiconductor nanoparticles of various shapes,[19-23] metal-organic frameworks,[24, 25] powders of single-source molecular precursors[26] and so forth. In EPD, the electrophoresis phenomenon is used to deposit charged particles from a suspension using an external electric field (E). Our group and others described the formation of CN films through EPD.[27] Nevertheless, despite the successful deposition of CN nanosheets, the large size of the CN sheets along with their low solubility in common solvents resulted in a poor physical connection to the substrate's surface, which strongly hinders the electronic conductivity from the layer to the conductive substrate.

Here we report the large-scale fabrication of CN films by using supramolecular assemblies composed from CN monomers as a seeding layer for the deposition of melamine vapor. For the growth of the seeding layer, we used EPD to deposit cyanuric acid–melamine supramolecular complexes.[28] This new deposition method enables good control over the CN thickness as well as its photophysical and structural properties. The CN films exhibit good photoelectrochemical activity owing to a strong adhesion to the substrate and the formation of an electronic heterojunction. We believe this is one of the synthetic tools that can be harnessed to allow fabrication of metal-free CN-based photoanodes for PEC.

An illustration of the fabrication of the CN electrode by using an EPD method assisted by vapor deposition is presented in Scheme 1. First, cyanuric acid–melamine (CM) supramolecular complexes were prepared by mixing the precursors in water
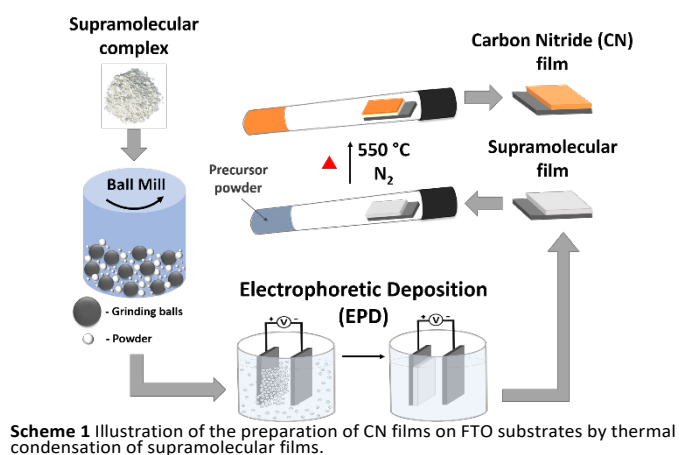
Scheme 1 Illustration of the preparation of CN films on FTO substrates by thermal condensation of supramolecular films.

Fig. 1 (a) Digital image of CM_x electrodes (where x is the deposition time, 5–180 s). (b) Top-view SEM image of CM_{120} electrode. (c) XRD patterns of CM powders (assembled in water) before (orange) and after (pink) ball-milling, a CM_{120} electrode (purple) and a clean FTO reference (gray). (d) Film thickness of CM_x electrodes as function of deposition time, determined by laser microscopy (see details in Fig. S4 and Table S1).

(1:1 molar ratio), resulting in a powdery precipitate.[29] A stable colloidal suspension for EPD was obtained by ball-milling the CM powder to ensure dispersion and narrower size distribution in toluene as the dispersion medium.

Homogenous white CM complexes were deposited on FTO-coated glass substrates *via* EPD by applying a constant potential bias of 300 V between the two electrode substrates, dipped in the suspension, for varying time periods (5, 30, 60, 120 and 180 s). Ball-milled (bm) CM particles were deposited on the positively-biased electrode, which indicates that the CM colloids are negatively charged (visualized in Movie S1 "EPD process of bm-CM complex").

Scanning electron microscopy (SEM) images show that the rod-like structure of the CM powder assembled in water has completely changed after ball milling,[30] which resulted in nanometric-sized particles that assembled into aggregates (Fig. S1 in the ESI). SEM top-view images of the CM_x electrodes (Fig. 1a, where x represents the deposition time in s) show how the aggregates are successfully deposited on FTO glass (Fig. 1b and Fig. S2).

The preservation of the CM supramolecular complexes' structure after deposition on FTO was confirmed by X-ray diffraction (XRD) and Fourier-transform infrared (FTIR) analyses. Compared to the CM powder, XRD patterns of the bm-CM powder as well as CM_{120} electrode (which was chosen as a case study due to its enhanced photoelectrochemical performance as will be discussed later) display two broader peaks, at $2\theta =$ 10.67° (100) and 27.9° (002) (Fig. 1c), attributed to in-planar packing and graphite-like stacking, respectively.[31] The reduction of diffraction signals around 27° after ball-milling indicates that the CM particles are more orientated to one direction.[32] The typical peaks in the FTIR spectra of CM arising from the C=O vibration peaks at 1656 cm^{-1} and 1725 cm^{-1}, and the triazine ring vibration peak at 763 cm^{-1} (Fig. S3), further support the successful CM film formation on FTO.

Altering EPD times allowed control over the film thickness (Fig. 1d and Fig. S4). A clear correlation between the film thickness and the deposition time is observed for time intervals shorter than 60 s; it is further supported by preparation of three additional CM electrodes: $CM_{2,15,45}$ (Fig. S5). Once deposition time reaches 60 s, the average film thickness stabilizes around
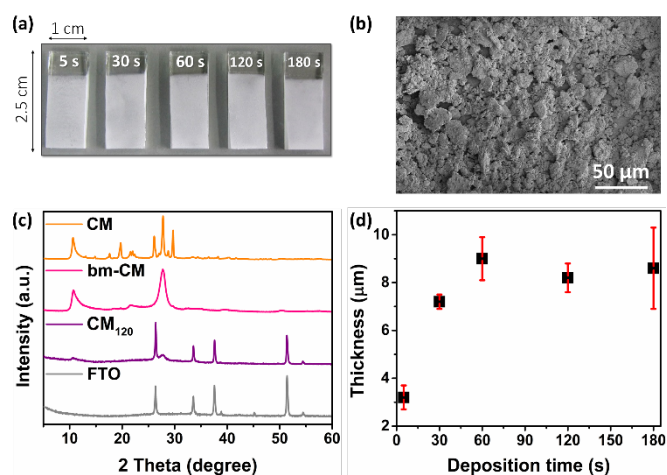
8.7 µm (Table S1) as aggregates start falling from the substrate, at the end of the deposition, as the electrode is pulled out of the suspension (visualized in Movie S1). The maximum measured thickness is approximately 10 µm (top of the error bars). From these measurements we conclude that 120 s is the optimal deposition time, as CM_{120} displays a relatively thick film with small standard deviation. Once the control over the supramolecular film thickness was established, this film was applied as the seeding layer in order to form CN films upon thermal condensation.

CN electrodes were formed by heating the CM_x electrodes at 550 °C under N_2 atmosphere together with 1.0 g of melamine powder (M), at the closed edge of the tube without direct contact with the CN electrode (Scheme 1). During calcination, M vapor is deposited on the formed CM films, which act as nucleation centers (*i.e.*, a seeding layer) for the growth of the final CN films. In this manner, uniform yellow CN films were obtained on top of the FTO (Fig. 2a), labeled as CN-CM_xM electrodes. The addition of M as a CN precursor displays a crucial role, as in its absence only a very thin CN film was formed, and most of the supramolecular film has evaporated completely during the thermal treatment.

SEM images of CN-CM_{120}M electrode (Fig. 2b–c) as well as top-view SEM images of CN-CM_xM electrodes (Fig. S6) show the attachment of large M-CN features on top of the film as a result
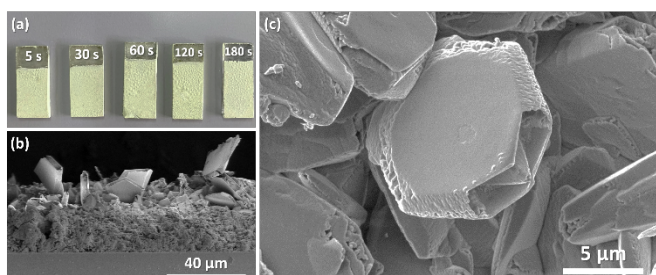

Fig. 2 CN films formed after a thermal treatment. (a) Digital photo of the final CN-CM_xM electrodes. (b) Cross-sectional and (c) top-view SEM images of CN-CM_{120}M electrode.

of melamine vapor deposition. Cross-sectional SEM images of CN-CM$_x$M electrodes suggest the formation of a compact film with a strong adhesion of the CN to the FTO (Fig. S7a).

High-magnification cross-sectional SEM images of CN-CM$_{120}$M electrode show the direct growth of the CN film on top of the FTO coating (~350 nm) without evidence of the formation of two different layers (Fig. S7b–c). The latter implies that the CM film mainly provides a seeding layer for the growth of CN films.

To clarify the importance of the addition of M powder as well as to show that the supramolecular film acts as a seeding layer for the formation of CN films, CM$_{60}$ (the thickest supramolecular film) without the addition of M powder and a bare FTO electrode with 1.0 g of M powder were subjected to the same calcination procedure as the CN-CM$_x$M, and were labeled CN-CM$_{60}$ and CN-M, respectively. SEM images of CN-CM$_{60}$ (Fig. S8a) show a very poor CN coating on the FTO, while CN-M exhibits a highly disordered coating with flower-like microstructures[33] of calcined melamine directly on top of the FTO (Fig. S8b). These results emphasize the synergetic effect of the seeding layer together with a CN precursor in order to grow CN films.

XRD patterns of CN-CM$_x$M show a strong peak attributed to the interplanar stacking (002) peak at 27.5° and a relatively weak in-planar (100) peak at around 13.4° (Fig. 3a), both correspond to the structure of layered polymeric CN materials. FTIR spectra reveal stretching modes of CN heterocycles in the 1200–1600 cm^{-1} range, while the peak at 800 cm^{-1} is attributed to the breathing vibration of the tri-s-triazine unit and the peak at around 3000 cm^{-1} belongs to N–H stretching (Fig. 3b) confirming the formation of CN films.

C1s XPS spectra (Fig. S9a) of CN-CM$_{120}$M electrode presents two different species corresponding to adventitious C–C and N=C–N coordination at 284.8 eV and 288.1 eV, respectively. N1s XPS spectra (Fig. S9b) support the CN formation as four deconvoluted peaks at 398.5 eV, 399.8 eV, 401.2 eV and 404.2 eV correspond to C=N–C, N–C$_3$, C–NH$_2$ and charging effects, respectively.

The final CN film thickness was affected by varying the deposition time of the supramolecular assemblies (Fig. 3c, Fig. S10 and Table S2). The same trend that was observed in CM films can be seen also in the CN-CM$_x$M electrodes, excluding CN-CM$_{180}$M, which was significantly thicker than the other electrodes, probably due to the high roughness of its seeding layer (expressed by the large standard deviation of the CM$_{180}$ film). In order to investigate the effect of melamine vapor deposition during the calcination of the seeding layer, CM$_{60}$ electrodes with different amounts of melamine powder (0.2, 0.4, 0.6 and 0.8 g) were prepared. Thicker CN-CM$_{60}$M$_y$ films (where y represents the melamine mass in g) were obtained in almost a linear manner when a higher melamine powder mass was presented in the reaction tube (Fig. S11 and Table S3).

The EPD process enables an easy scaled-up formation of CN films assisted with melamine sublimation during calcination. As exemplified in Fig. 3d, a large CN film was deposited on 1 × 9 cm^2 (width × length) FTO.
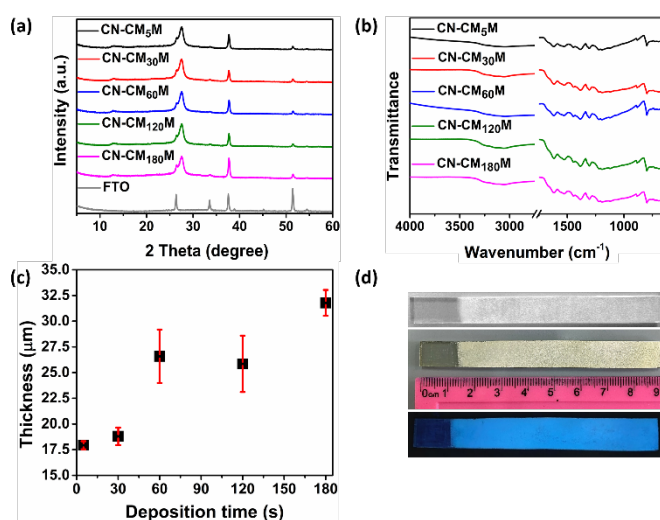

Fig. 3 (a) XRD patterns and (b) FTIR spectra of CN-CM$_x$M electrodes. (c) Film thickness of CN-CM$_x$M electrodes as function of deposition time. (d) Digital photos of 1 × 9 cm^2 electrodes before (CM$_{60}$, white) and after calcination at 550 °C without (CN-CM$_{60}$M, yellow) and under UV (365 nm) excitation (CN-CM$_{60}$M, lighted in blue).

The absorption spectra (Fig. 4a) of the CN-CM$_x$M electrodes show almost the same absorption onset *ca.* 480 nm, which corresponds to a bandgap of about 2.58 eV (calculated using a Tauc plot analysis, Fig. S12). The electrodes formed using 60–180 s EPD (*i.e.*, CN-CM$_x$M, x = 60, 120, 180) presented a higher optical density due to increased film thickness. The photoluminescence (PL) spectra of the CN-CM$_x$M electrodes indicate an emission peak at ~460 nm with no significant changes between the electrodes (Fig. 4b).

As a proof of concept for the generality of this method (seeding layer together with CN precursor vapor), a CN-CM$_{120}$CM electrode (CM$_{120}$ electrode calcined together with 1.0 g of CM powder) was prepared. SEM images resemble a more porous but less robust and compact film compared to CN-CM$_{120}$M (Fig. S13). The UV-vis absorption curve of CN-CM$_{120}$CM electrode is slightly blue-shifted compared to CN-CM$_{120}$M electrode (Fig. S14a), corresponding to a wider band gap of 2.68 eV compared to 2.56 eV of the electrode prepared with M powder as the vapor deposition source (Fig. S14b). Photoluminescence spectra of the CN-CM$_{120}$CM show significant quenching relative to the CN-CM$_{120}$M (Fig. S14c).

The prepared CN-CM$_x$M electrodes were tested as photoanodes in PEC water-splitting using a standard three electrode setup.[11] Photocurrent density was measured at 1.23 V *vs.* reversible hydrogen electrode (RHE) in 0.1 M KOH in the dark and under one-sun illumination using both front- and back-side illumination. Illuminating from the back results in higher photocurrent densities compared to front-side by about 20 µA cm^{-2} for all electrodes. This phenomenon probably stands for a non-optimal layer thickness which leads to a shorter required electron diffusion length in the case of back-illumination (Fig. S15a–e). A comparison between the electrodes under back-side illumination reveals that CN-CM$_{60}$M and CN-CM$_{120}$M have the highest photocurrent density of approximately 47 µA cm^{-2} (Fig. S15f). In addition, compared to CN-CM$_{120}$M, the photocurrent density of the CN-CM$_{120}$CM electrode shows low stability and a
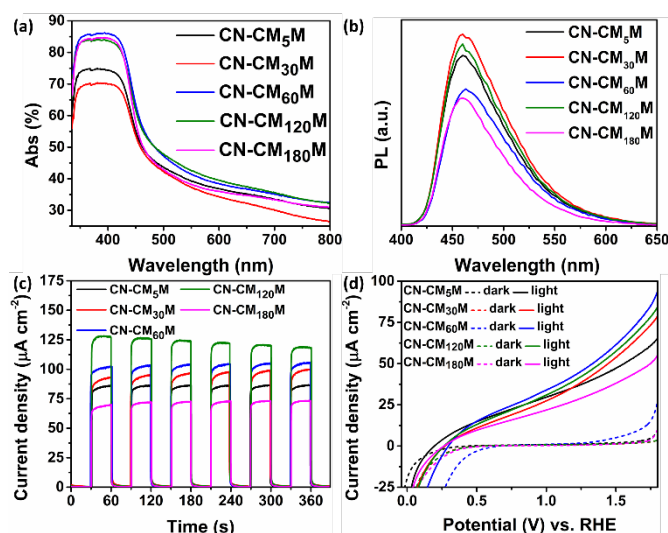
Fig. 4 Optical characterization of CN-CM$_x$M electrodes. (a) UV-vis absorption spectra, and (b) photoluminescence spectra (λ_{ex} = 380 nm). (c) Photocurrent densities of CN-CM$_x$M electrodes at 1.23 V *vs.* RHE in 0.1 M KOH aqueous solution containing 10% v/v TEOA hole scavenger upon on/off back-side illumination (1 sun). (d) LSV curves of CN-CM$_x$M electrode in 0.1 M KOH aqueous solution in the dark (dashed) and under back-side illumination (1 sun, complete lines).

sharp decay (Fig. S16). We note, that the current performances of CN electrodes in PEC are still low compared to the state-of-art semiconductors owing to the limited light harvesting and charge separation properties.[34-36]

With the addition of triethanolamine (10% v/v TEOA in 0.1 M KOH) acting as a hole scavenger, the electrodes showed higher photocurrent densities and certain improvement in the stability (Fig. 4c). CN-CM$_{120}$M achieved the highest photocurrent density of about 122 μA cm^{-2}. As the difference in the thickness between CN-CM$_{60}$M and CN-CM$_{120}$M is insignificant (26.6 and 25.9 μm, respectively), the photocurrent densities were relatively similar (122 and 104 μA cm^{-2}). CN-CN$_{180}$M showed the lowest photocurrent density, which we ascribe to the thicker film (31.8 μm), which hinders the performance, probably due to increased recombination in the bulk and decreased conductivity. Long-term stability tests under the same conditions show that more than 70% of the initial photocurrent of the CN-CM$_x$M electrodes is preserved after 3 h of continuous illumination (Fig. S17).

Linear sweep voltammetry (LSV) curves in the dark and under one-sun illumination in 0.1 M KOH aqueous solutions (pH ≈ 13) exhibit a typical PEC behavior (Fig. 4d). The obtained low onset potentials reveal that the photocurrent starts ~1 V below the 'dark' thermodynamic water oxidation potential (1.23 V *vs.* RHE).

Mott-Schottky analysis (Fig. S18) for CN-CM$_x$M and CN-CM$_{120}$CM electrodes indicates an n-type semiconductor behavior. The flat band (FB) potentials of the electrodes were estimated from the extrapolated linear fits that intercept the *x*-axis (potential (V) *vs.* RHE). The full band position diagrams determined from the optical analysis and the Mott–Schottky measurements (Fig. S19) reveal that all the electrodes are suitable for water reduction and oxidation.

The incident photon-to-current conversion efficiency (IPCE) measurement at 1.23 V *vs.* RHE of the CN-CM$_{120}$M electrode with and without the addition of hole scavenger at different wavelengths has revealed that the photoresponse onset is expanded into the visible region, up to 450 nm, as the 480 nm shows a negligible photoresponse (Fig. S20) owing to the direct band gap of CN materials. The maximum efficiency with 10% (v/v) TEOA was calculated to be 1.8% at 400 nm compared to 1.1% without.

The H$_2$ generation in the presence of TEOA in 0.1 M KOH solution was tracked using gas chromatography (GC) (see Fig. S21). The CN-CM$_{120}$M photoanode achieved a H$_2$ generation rate of 0.55 mmol g^{-1} h^{-1}. The overall Faraday efficiency (FE) for CN-CM$_{120}$M at 3 h is 74.9%.

Conclusions

To conclude, we demonstrated a facile and scalable growth technique of carbon nitride films using a supramolecular complex composed of CN monomers as a seeding layer on FTO followed by the controlled growth of CN by vapor deposition means. The successful seeding layer deposition was achieved by using electrophoretic deposition of supramolecular complexes, resulting in good control over the layer thickness and composition. The use of seeding layers for the CN growth enables good adhesion to the substrate and improved photoelectrochemical properties as well as unique electronic structure.

Conflicts of interest

There are no conflicts to declare.

Acknowledgements

References

1.   Y. Zheng, J. Liu, J. Liang, M. Jaroniec and S. Z. Qiao, *Energy Environ. Sci.*, 2012, **5**, 6717-6731.

2.   Y. Wang, X. Wang and M. Antonietti, *Angew. Chem. Int. Ed.*, 2012, **51**, 68-89.

3.   A. Savateev, I. Ghosh, B. König and M. Antonietti, *Angewandte Chemie International Edition*, 2018, **57**, 15936-15947.

4. F. K. Kessler, Y. Zheng, D. Schwarz, C. Merschjann, W. Schnick, X. Wang and M. J. Bojdys, *Nature Reviews Materials*, 2017, **2**, 17030.

5. S. Cao, J. Low, J. Yu and M. Jaroniec, *Adv. Mater.*, 2015, **27**, 2150-2176.

6. W. J. Ong, L. L. Tan, Y. H. Ng, S. T. Yong and S. P. Chai, *Chem Rev*, 2016, **116**, 7159-7329.

7. Y. Zheng, L. Lin, B. Wang and X. Wang, *Angew. Chem. Int. Ed.*, 2015, **54**, 12868-12884.

8. Z. Zhou, Y. Zhang, Y. Shen, S. Liu and Y. Zhang, *Chemical Society Reviews*, 2018, **47**, 2298-2321.

9. J. Safaei, N. A. Mohamed, M. F. Mohamad Noh, M. F. Soh, N. A. Ludin, M. A. Ibrahim, W. N. Roslam Wan Isahak and M. A. Mat Teridi, *Journal of Materials Chemistry A*, 2018, **6**, 22346-22380.

10. Q. Ruan, M. K. Bayazit, V. Kiran, J. Xie, Y. Wang and J. Tang, *Chemical Communications*, 2019, **55**, 7191-7194.

11. M. Volokh, G. Peng, J. Barrio and M. Shalom, *Angew. Chem. Int. Ed.*, 2019, **58**, 6138-6151.

12. J. Xu, T. J. K. Brenner, L. Chabanne, D. Neher, M. Antonietti and M. Shalom, *J. Am. Chem. Soc.*, 2014, **136**, 13486-13489.

13. Q. Ruan, W. Luo, J. Xie, Y. Wang, X. Liu, Z. Bai, C. J. Carmalt and J. Tang, *Angew. Chem. Int. Ed.*, 2017, **56**, 8221-8225.

14. J. Bian, Q. Li, C. Huang, J. Li, Y. Guo, M. Zaw and R.-Q. Zhang, *Nano Energy*, 2015, **15**, 353-361.

15. K. Wu and I. Zhitomirsky, *International Journal of Applied Ceramic Technology*, 2011, **8**, 920-927.

16. L. Besra and M. Liu, *Prog. Mater Sci.*, 2007, **52**, 1-61.

17. A. R. Boccaccini, J. Cho, J. A. Roether, B. J. C. Thomas, E. Jane Minay and M. S. P. Shaffer, *Carbon*, 2006, **44**, 3149-3160.

18. Z.-S. Wu, S. Pei, W. Ren, D. Tang, L. Gao, B. Liu, F. Li, C. Liu and H.-M. Cheng, *Adv. Mater.*, 2009, **21**, 1756-1760.

19. M. Fayette, A. Nelson and R. D. Robinson, *J. Mater. Chem. A*, 2015, **3**, 4274-4283.

20. J. Liu, Z. Wu, T. Li, D. Zhou, K. Zhang, Y. Sheng, J. Cui, H. Zhang and B. Yang, *Nanoscale*, 2016, **8**, 395-402.

21. A. Salant, M. Shalom, I. Hod, A. Faust, A. Zaban and U. Banin, *ACS Nano*, 2010, **4**, 5962-5968.

22. A. Vázquez, I. A. López and I. Gómez, *Journal of Materials Science*, 2013, **48**, 2701-2704.

23. S. L. Allen and F. P. Zamborini, *Langmuir : the ACS journal of surfaces and colloids*, 2019, **35**, 2137-2145.

24. I. Hod, W. Bury, D. M. Karlin, P. Deria, C.-W. Kung, M. J. Katz, M. So, B. Klahr, D. Jin, Y.-W. Chung, T. W. Odom, O. K. Farha and J. T. Hupp, *Adv. Mater.*, 2014, **26**, 6295-6300.

25. I. Liberman, W. He, R. Shimoni, R. Ifraemov and I. Hod, *Chemical Science*, 2020, **11**, 180-185.

26. M. Volokh, M. Diab, K. Flomin and T. Mokari, *J. Colloid Interface Sci.*, 2018, **515**, 221-231.

27. J. Xu and M. Shalom, *ACS Appl Mater Interfaces*, 2016, **8**, 13058-13063.

28. J. Barrio and M. Shalom, *ChemCatChem*, 2018, **10**, 5573-5586.

29. M. Shalom, M. Guttentag, C. Fettkenhauer, S. Inal, D. Neher, A. Llobet and M. Antonietti, *Chemistry of Materials*, 2014, **26**, 5812-5818.

30. S. Dolai, J. Barrio, G. Peng, A. Grafmüller and M. Shalom, *Nanoscale*, 2019, **11**, 5564-5570.

31. Y.-S. Jun, E. Z. Lee, X. Wang, W. H. Hong, G. D. Stucky and A. Thomas, *Adv. Funct. Mater.*, 2013, **23**, 3661-3667.

32. J. Barrio, L. Lin, X. Wang and M. Shalom, *ACS Sustainable Chemistry & Engineering*, 2018, **6**, 519-530.

33. W. Xiong, F. Huang and R.-Q. Zhang, *Sustainable Energy & Fuels*, 2020, **4**, 485-503.

34. Y. Fang, X. Li and X. Wang, *ACS Catalysis*, 2018, **8**, 8774-8780.

35. Y. Fang, X. Li and X. Wang, *ChemSusChem*, 2019, **12**, 2605-2608.

36. Y. Fang, X. Li, Y. Wang, C. Giordano and X. Wang, *Appl. Catal., B*, 2020, **268**, 118398.

Electronic Supplementary Information

Electrophoretic deposition of supramolecular complexes for the formation of carbon nitride films

*Liel Abisdris[a], Jonathan Tzadikov[a], Neeta Karjule[a], Adi Azoulay[a], Michael Volokh[a], Menny Shalom[*a]*

a. Department of Chemistry and Ilse Katz Institute for Nanoscale Science and Technology, Ben-Gurion University of the Negev, Beer-Sheva 8410501, Israel.
*E-mail: mennysh@bgu.ac.il

Experimental

Materials

All reagents and solvents (abbreviation, purity, manufacturer) were used as received: cyanuric acid (CA, 98%, Merck), melamine (M, 99%, Sigma-Aldrich), toluene (AR, LOBA Chemie), potassium hydroxide pellets (KOH, AR, 85%, LOBA Chemie), sodium sulphate anhydrous (Na_2SO_4, AR, 99%, Loba Chemie), and triethanolamine (TEOA, $\geq$ 99.0%, Glentham Life Sciences). Deionized water (18.2 MΩ cm resistivity at 25 °C, purified using a Merck Millipore Direct-Q3 system) was used for all aqueous solutions. Fluorine-doped tin oxide coated glass (FTO, 12–14 Ω sq^{-1}, Xop Glass company – Spain) was cut, washed with an aqueous detergent solution (1% w/v Alconox), and sonicated for 20 min with acetone (AR, Bio-Lab) and ethanol (AR, Macron Fine Chemicals), subsequently.

Supramolecular precursor synthesis

A cyanuric acid–melamine (CM) supramolecular complex was prepared by mixing equal amounts of CA and M (4 mmol) in 30 mL water. The mixture was shaken for 2 h, centrifuged and dried for 24 h at 60 °C in a vacuum oven, resulting in a CM powder.

Supramolecular-films preparation

CM powder was ground for 45 min using Fritsch Pulverisette 7 planetary ball mill (3 mm ZrO_2 balls, dry milling), washed with water, centrifuged, and dried for 24 hours at 60 °C in a vacuum oven. Next, 50 mg of ball-milled CM powder was dispersed in 5 mL of toluene to form a stable colloidal suspension (10 mg mL^{-1}). The obtained suspension was used as the deposition medium for forming CM films on top of FTO by electrophoretic deposition (EPD). The EPD setup consisted of two FTOs dipped into the deposition medium in a parallel capacitor configuration, *i.e.*, the FTO electrodes in the suspension were connected to a DC voltage using an ENDURO power supply. A constant voltage of 300 V was applied during the deposition for 2 s, 5 s, 15 s, 30 s, 45 s, 60 s, 120 s, and 180 s.

CN-films formation

Each CM_x (x = 2, 5, 15, 30, 45, 60, 120, and 180 s) electrode was placed in a glass tube (16 mm diameter × 100 mm length) along with 1.0 g melamine as a CN precursor powder for the vapor deposition. The tube was purged with N_2 for several seconds and covered tightly with an Al foil. The electrodes in each tube were calcined under N_2 atmosphere (constant flow rate of 120 mL min^{-1}), to 550 °C with a heating ramp of 5 °C min^{-1} and kept for 4 h, resulting in CN-CM_xM electrodes. In the same calcination conditions, CM_{120} electrode with CM powder (1.0 g), which was used as a CN precursor powder instead of melamine, was prepared, forming CN-$CM_{120}CM$ electrode, and CM_{60} electrodes with different amounts of melamine powder were prepared, forming CN-$CM_{60}M_y$ electrodes (y = 0.2, 0.4, 0.6 and 0.8 g).

Characterization

FTIR spectra were obtained by using a Thermo Scientific Nicolet iS5 in the 650–4000 cm^{-1} range using a diamond iD7 ATR. UV-vis spectra were acquired using a Cary 100 spectrophotometer equipped with a DRA (integrating sphere), in transmittance (T) and reflectance (R) modes, while the *Abs*(%) has calculated according to 100% – T(%) – R(%). Photoluminescence spectra were measured by using Edinburgh instruments FLS920P Fluorimeter with an excitation wavelength of λ_{ex} = 380 nm. Digital photos under UV (365 nm) illumination were taken using a TLC viewing cabinet Vilber-Lourmat CN-6. X-ray diffraction patterns (XRD) were recorded on a PANalytical's Empyrean Diffractometer equipped with a position sensitive detector X'Celerator. The data was collected for 2θ ranging from 5° to 60°, with a scanning time of ~7 min using Cu Kα radiation (λ = 1.54178 Å, 40 kV, 30 mA). XPS data was collected by using an X-ray photoelectron spectrometer (Thermo Fisher ESCALAB 250) ultrahigh vacuum (1×10^{-9} bar) with an Al Kα X-ray source and a monochromator. The X-ray beam size was 500 μm and survey spectra was recorded with a pass energy (PE) of 150 eV and high energy resolution spectra were recorded with a PE of 20 eV. All XPS spectra peaks were shifted relative to the C 1s peak, positioned at 284.8 eV, to correct for charging effects. The XPS results were analyzed by using the AVANTGE software. For measuring film thickness, the electrodes were scratched in three different areas on top of the same film, using a needle (1.20 mm diameter). Thickness profile was obtained by using a 3D laser microscope (LEXT OLS5000), under low magnification (×10), *via* focusing on a specific scan area around the scratches. The roughness from both sides of the scratch (300

× 200 μm) was averaged by the software, then the distance between the lowest part (FTO level), to the averaged top part of the coating (to the left and right of the scratch) has been calculated. Scanning electron microscopy (SEM) images were recorded on an FEI Verios 460L high resolution SEM, operated at 3.0 kV, and equipped with a FEG source. To avoid charging effects, the samples were coated with 10 nm of sputtered gold (for CN precursors) or a carbon (for CN).

Photoelectrochemical measurements

Photoelectrochemical analysis was performed using a three-electrode system coupled to PalmSens3 (chronoamperometry, linear sweep voltammetry) or Metrohm Autolab (Mott-Schotkky and IPCE) potentiostats. A Pt-plate (1.0 cm^2), and an Ag/AgCl (saturated KCl) electrodes were used as counter and reference electrodes, respectively. The electrolyte was either a 0.1 M KOH aqueous solution (pH ≈ 13) or a 0.1 M KOH solution containing 10% v/v TEOA as a hole scavenger. All the potentials *vs.* Ag/AgCl were converted with respect to a reversible hydrogen electrode (RHE), using the Nernst equation at room temperature:

$$E_{RHE}\ (V) = E_{Ag/AgCl}\ (V) + 0.197 + 0.059 \times pH$$

Chronoamperometry measurements were carried out at a bias potential of 1.23 V *vs.* RHE under one-sun illumination (power density of 100 mW cm^{-2}), provided by a solar simulator (Newport, OPS-A500, 300 W Xe arc lamp, equipped with an air mass AM 1.5G and water filters) and calibrated using a power meter (Newport, 919P thermopile detector). The electrolyte was purged with N$_2$ for 15 min, followed by linear sweep voltammetry (LSV) measurements in the dark and under 1 sun illumination, at a scan rate of 10 mV s^{-1}. Mott-Schottky measurements were performed in 1 M Na$_2$SO$_4$ at a 1.0 kHz frequency. Incident photon-to-current conversion efficiency (IPCE) values at different wavelengths were calculated from the following equation:

$$IPCE\ (\%) = \frac{J_{KOH-or-TEOA}\ (A\ cm^{-2}) \times 1240}{\lambda\ (nm) \times I\ (W\ cm^{-2})} \times 100\%$$

Where J is the photocurrent density (J_{KOH} is the photocurrent obtained in 0.1 M KOH aqueous solution, while J_{TEOA} is the photocurrent obtained in 0.1 M KOH aqueous solution

containing 10% (v/v) TEOA; λ is the wavelength of the incident monochromatic light (400, 420, 450, and 480 nm); I is the light power density. Incident monochromatic light of different wavelengths was obtained by inserting a corresponding band-pass filter (Newport 10BBPF10-400, 10BBPF10-420, 10BBPF10-450, and 10BBPF10-480) between the solar simulator and the PEC cell.

The amount of photogenerated H_2 in the reactor headspace was analyzed using a gas chromatograph (Agilent 7820 GC system) equipped with a thermal conductivity detector (TCD).

Faraday efficiency (FE) was calculated using the following equation:

$$FE\ (\%) = \frac{m \cdot n \cdot F}{I \cdot t} \times 100\%$$

Where m is the number of moles of gas actually produced; n is the number of electrons in the electrochemical reaction; F is the Faraday constant; I is photocurrent; t is reaction time. This equation represents the ratio between the actual hydrogen gas evolution rate and calculated one from measuring the generated photocurrent.
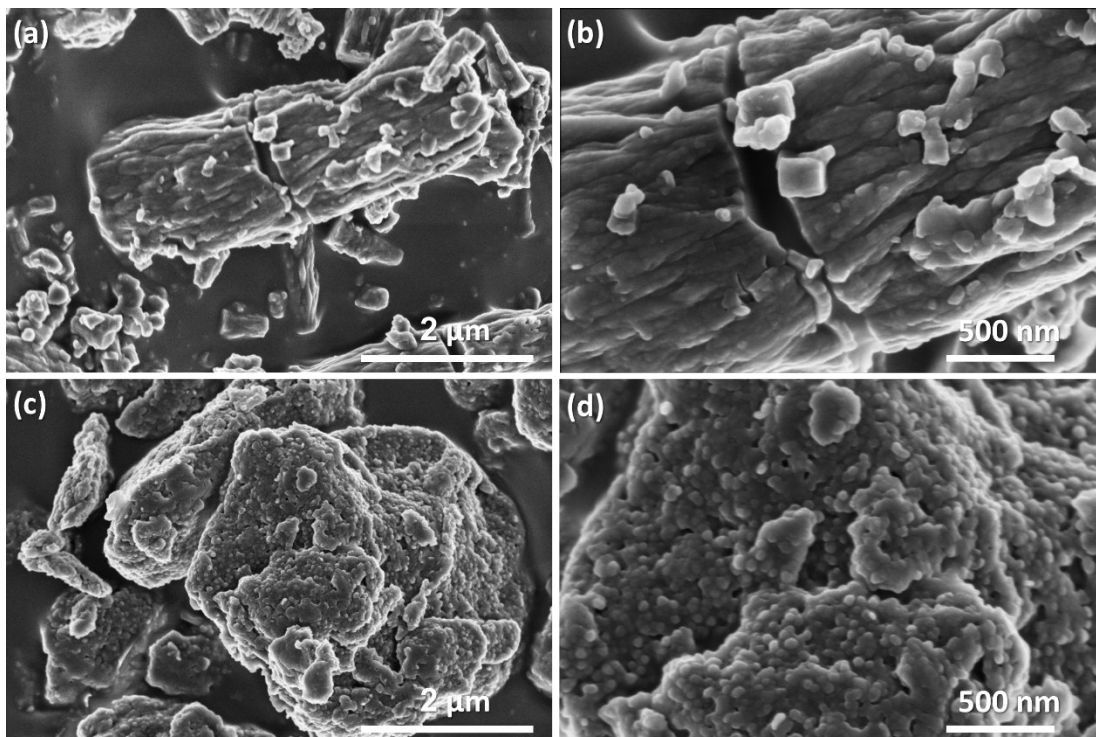
Fig. S1 SEM images of CM powder assembled in water (a)–(b) before and (c)–(d) after ball-milling.
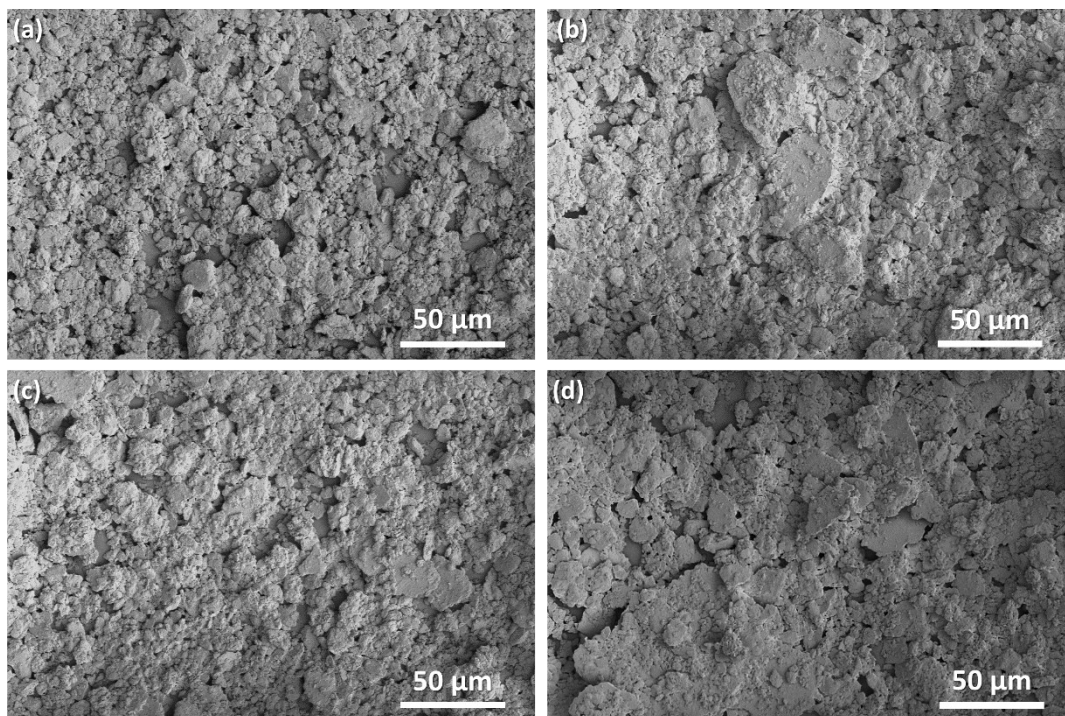
Fig. S2 Top-view SEM images of (a) CM_5, (b) CM_{30}, (c) CM_{60}, and (d) CM_{180} electrodes.
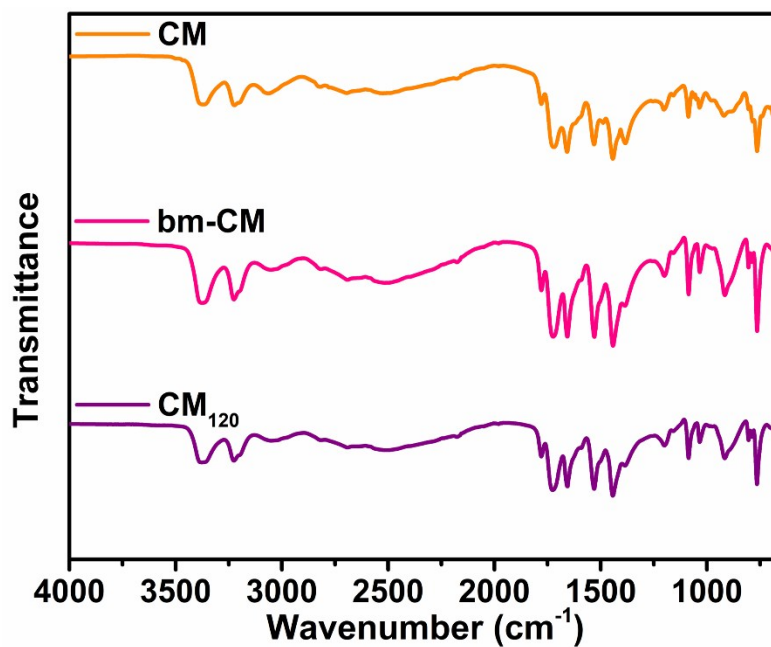
Fig. S3 FTIR spectra of CM powders (assembled in water) before (orange) and after (rose) ball milling, and CM_{120} electrode (purple). Spectra are offset for clarity.
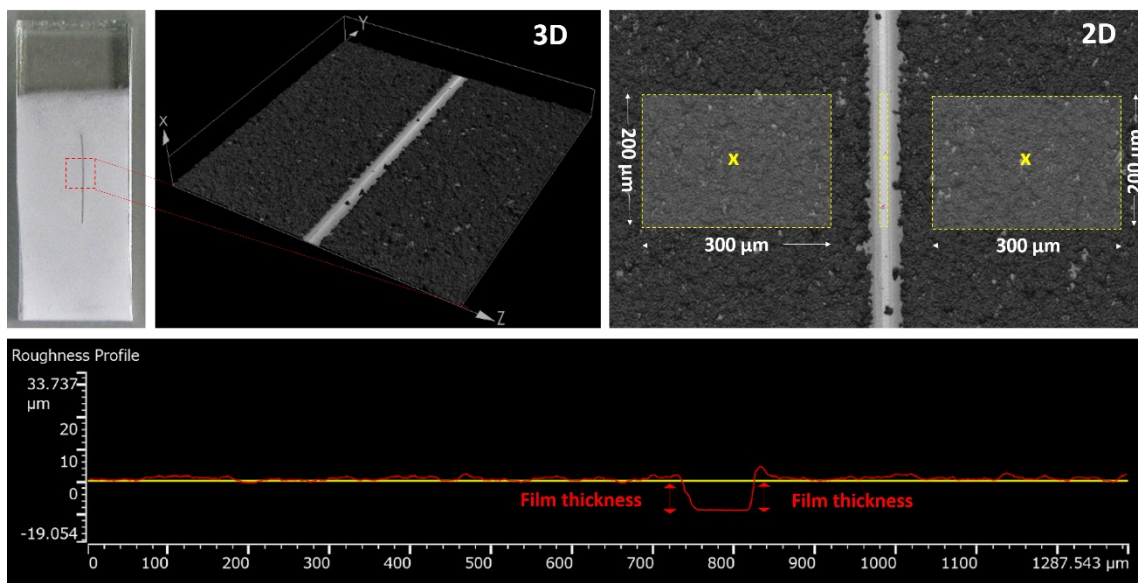
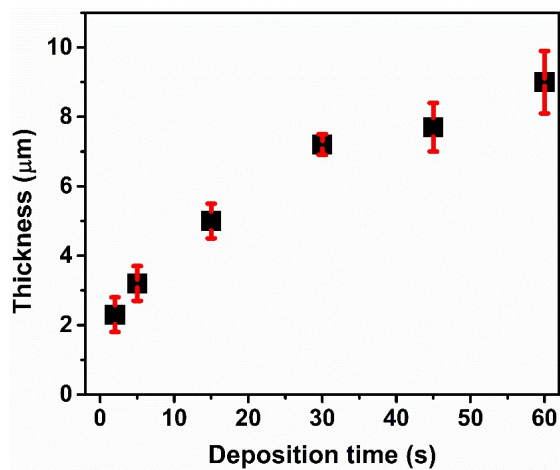**Fig. S4** General thickness profile of a CM_x electrode measured using a 3D laser microscope.

Fig. S5 Film thickness of the CM_x electrodes in EPD time intervals shorter than 60 s (*i.e.*, $x = 2$, 5, 15, 30, 45, 60) as function of deposition time.

Table S1. Statistical calculations of CM_x films thickness.

Deposition time (s)	Average thickness of both sides (μm)	Total average thickness (μm)	Standard deviation (μm)
2	1.9	2.3	0.5
	2.8		
	2.1		
5	3.6	3.2	0.5
	2.6		
	3.3		
15	4.6	5.0	0.5
	5.5		
	4.9		
30	7.5	7.2	0.3
	7.1		
	7.0		
45	8.1	7.7	0.7
	8.1		
	6.9		
60	9.8	9.0	0.9
	8.1		
	9.3		
120	7.6	8.2	0.6
	8.3		
	8.8		
180	10.1	8.6	1.7
	9.0		
	6.8		
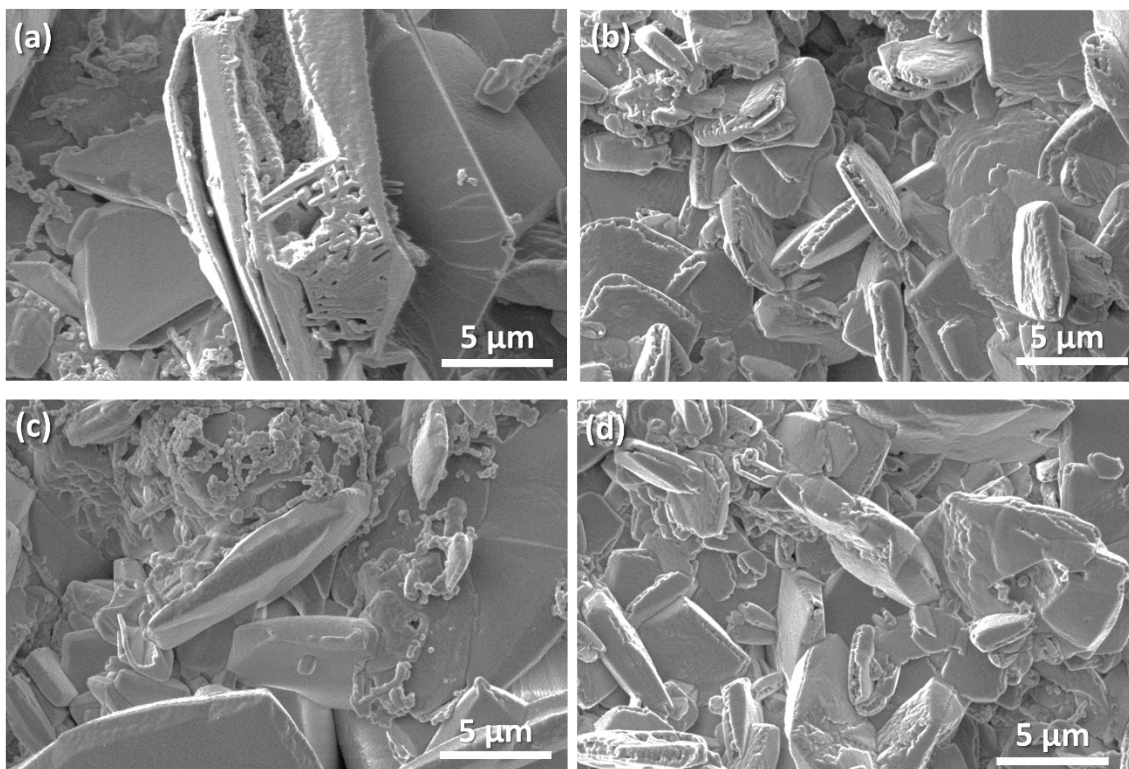
Fig. S6 Top-view SEM images of (a) CN-CM$_5$M, (b) CN-CM$_{30}$M, (c) CN-CM$_{60}$M, and (d) CN-CM$_{180}$M electrodes.
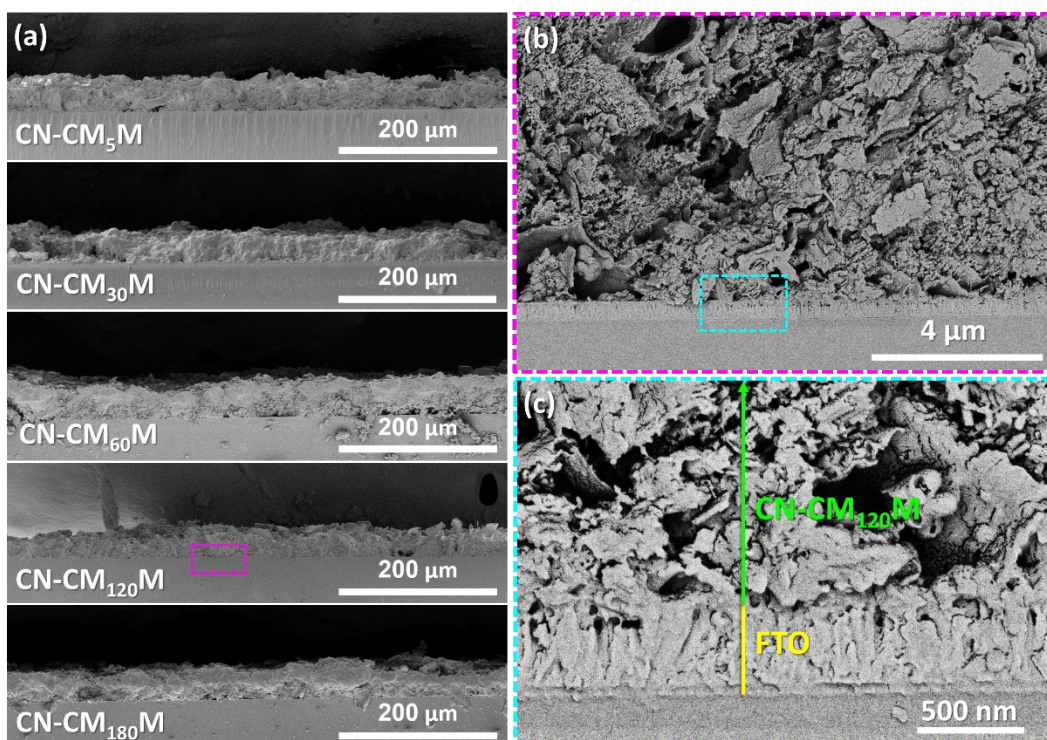
Fig. S7 Cross-sectional SEM images of (a) CN-CM$_x$M electrodes, and (b–c) CN-CM$_{120}$M.
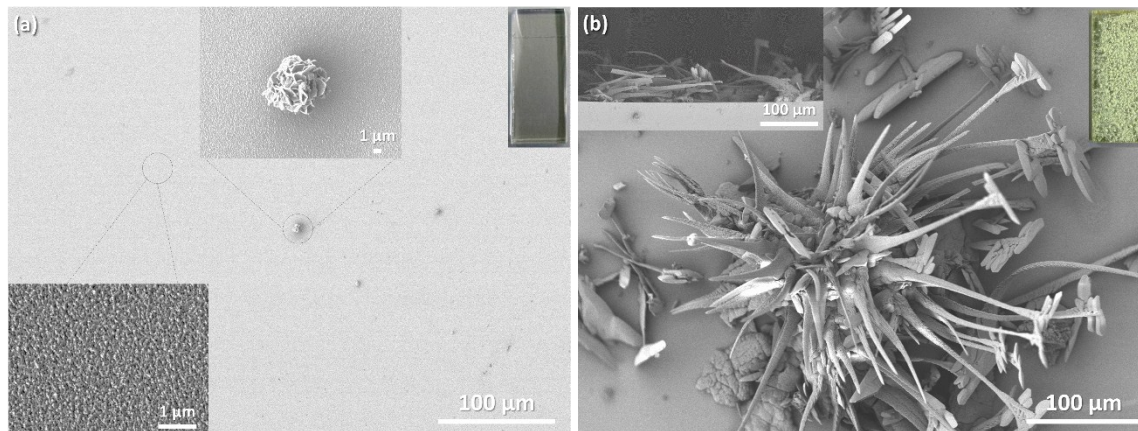
Fig. S8 Top-view SEM images of (a) CN-CM$_{60}$ (insets: the corresponding digital photo and top-view SEM images), and (b) CN-M (insets: the corresponding digital photo and cross-sectional SEM image) electrodes.
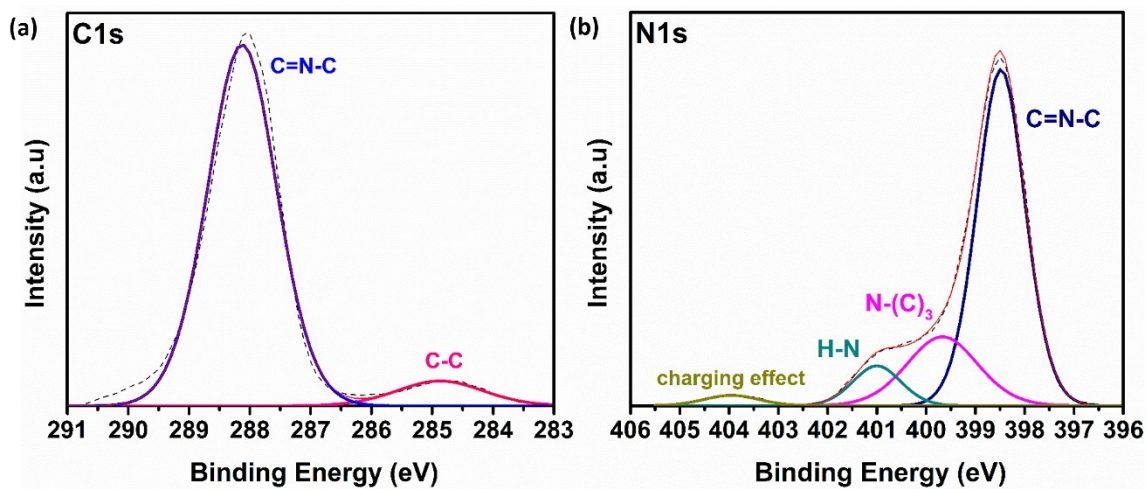
Fig. S9 XPS analysis of CN-CM$_{120}$M electrode for (a) C1s, and (b) N1s.
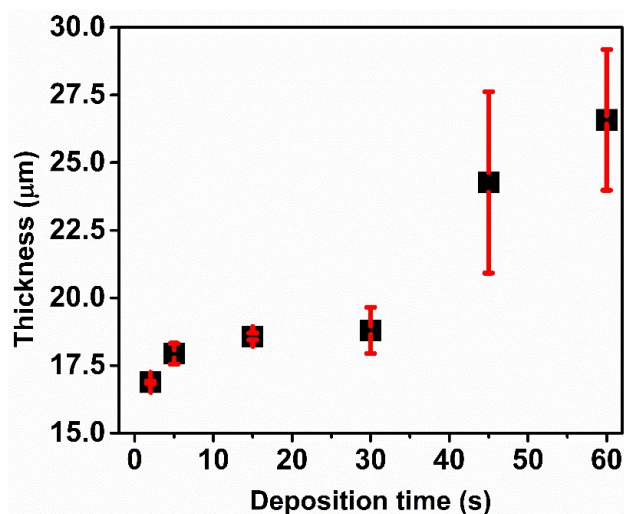
Fig. S10 Final film thickness of the CN-CM$_x$M electrodes (after calcination), which were prepared using EPD time intervals shorter than 60 s (*i.e.*, x = 2, 5, 15, 30, 45, 60) as function of deposition time.

Table S2. Statistical calculations of CN-CM$_x$M films thickness.

Deposition time (s)	Average thickness of both sides (μm)	Total average thickness (μm)	Standard deviation (μm)
2	16.8 16.9 16.9	16.9	0.05
5	17.6 17.1 19.2	17.9	1.1
15	18.5 18.5 18.7	18.6	0.1
30	19.7 18.7 18.0	18.8	0.9
45	20.4 25.8 26.6	24.3	3.4
60	29.2 24.0 26.6	26.6	2.6
120	27.2 22.7 27.7	25.9	2.7
180	32.1 32.9 30.4	31.8	1.3

S-11

Fig. S11 Film thickness of CN-CM$_{60}$M$_y$ electrodes as function of melamine powder mass in the glass tube during preparation of the electrodes.

Table S3.   Statistical calculations of CN-CM$_{60}$M$_y$ films thickness.

Melamine mass (g)	Average thickness of both sides (μm)	Total average thickness (μm)	Standard deviation (μm)
0.2	10.0 15.5 13.0	12.8	2.7
0.4	18.2 18.7 19.8	18.9	0.8
0.6	23.1 20.5 21.4	21.7	1.3
0.8	26.2 25.6 25.4	25.7	0.4
1.0	29.2 24.0 26.6	26.6	2.6

Fig. S12 Tauc plots of CN-CM$_x$M electrodes (direct optical band gap, E_g).
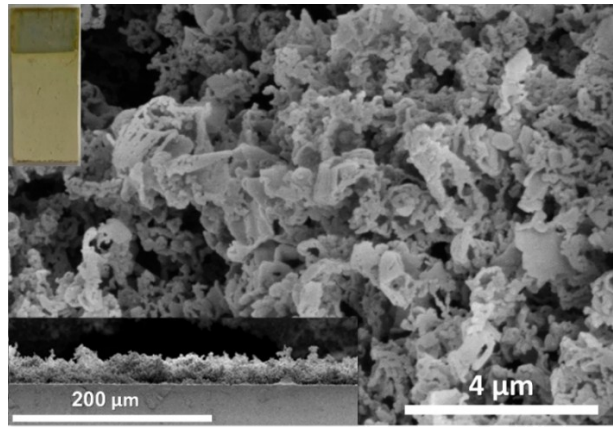
Fig. S13 SEM image of CN-CM$_{120}$CM electrode (insets: the corresponding digital photo and cross-sectional SEM image).
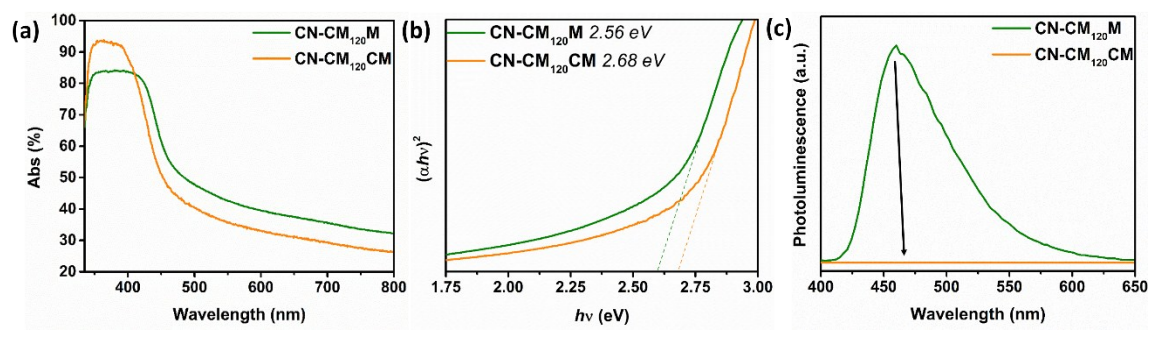
Fig. S14 Optical characterization of CN-CM$_{120}$CM and CN-CM$_{120}$M electrodes: (a) UV-Vis absorptance spectra, (b) Tauc plot analysis assuming a direct E_g, and (c) photoluminescence spectra (λ_{ex} = 380 nm).
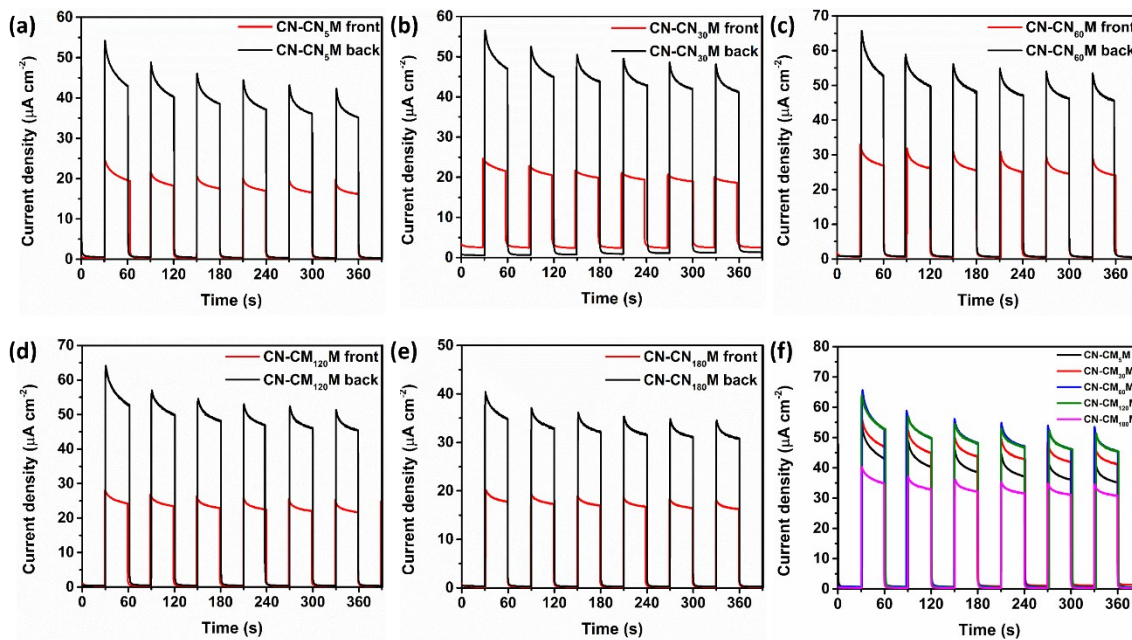
Fig. S15 Photocurrent densities at 1.23 V *vs.* RHE in 0.1 M KOH of (a) CN-CM$_5$M, (b) CN-CM$_{30}$M, (c) CN-CM$_{60}$M, (d) CN-CM$_{120}$M, and (e) CN-CM$_{180}$M electrodes under front- and back-illumination (1 sun), and (f) comparison of CN-CM$_x$M electrodes under back illumination (1 sun).
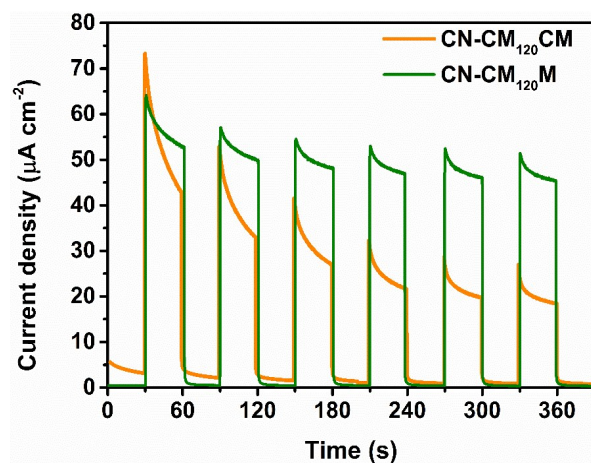
Fig. S16 Photocurrent densities of CN-CM$_{120}$CM and CN-CM$_{120}$M electrodes at 1.23 V *vs.* RHE in 0.1 M KOH under back-illumination (1 sun).
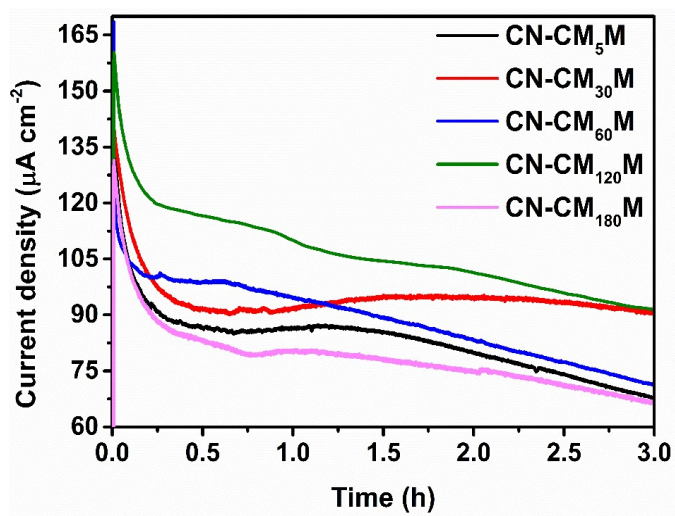

Fig. S17 Photocurrent stability of CN-CM$_x$M electrodes at 1.23 V *vs.* RHE in 0.1 M KOH aqueous solution containing 10% v/v TEOA upon continuous back-side illumination (1 sun).
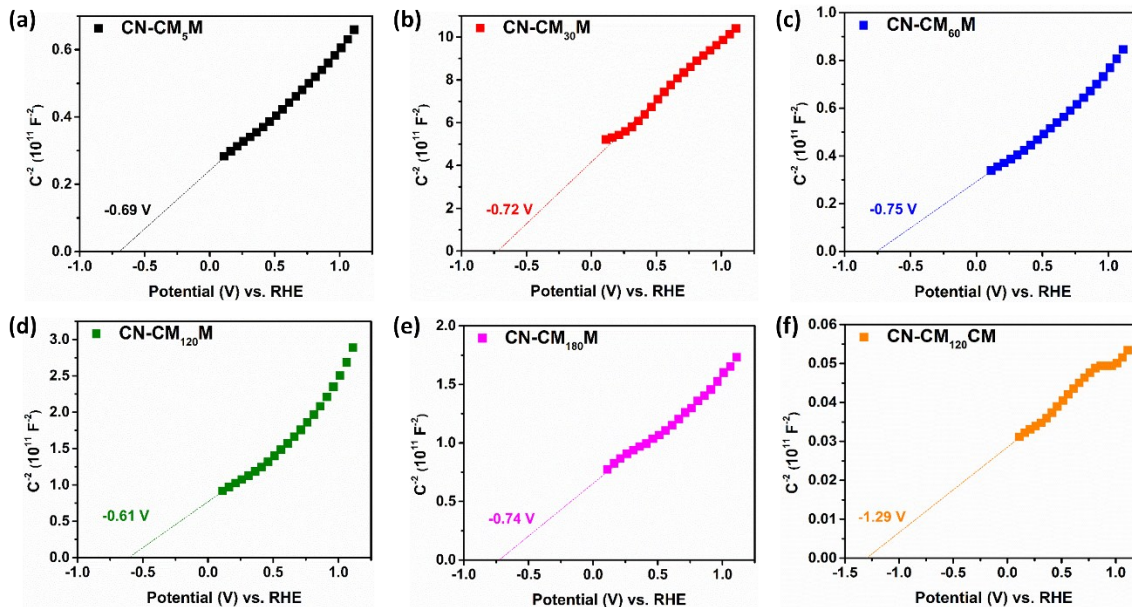
Fig. S18 Mott–Schottky plots of (a) CN-CM$_5$M, (b) CN-CM$_{30}$M, (c) CN-CM$_{60}$M, (d) CN-CM$_{120}$M, (e) CN-CM$_{180}$M, and (f) CN-CM$_{120}$CM electrodes.
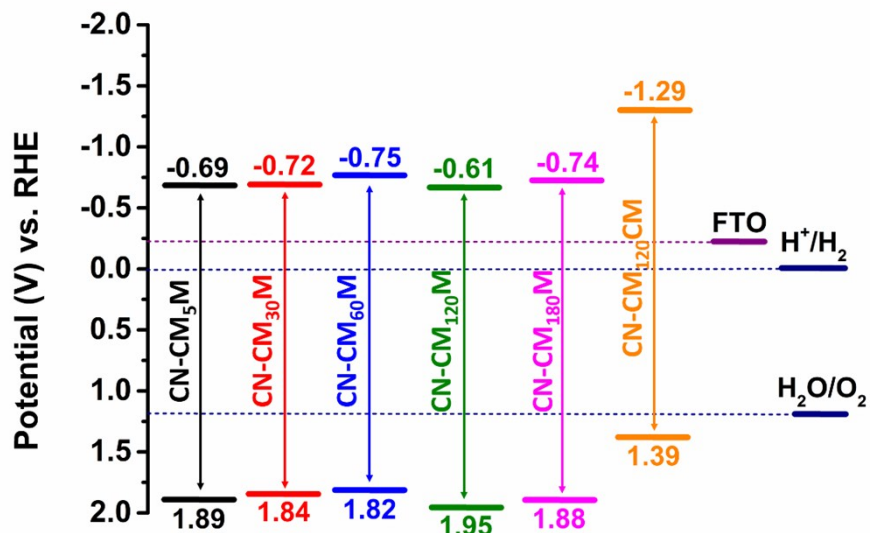

Fig. S19 Proposed energy level diagram of CN-CM$_x$M and CN-CM$_{120}$CM electrodes with respect to water redox reactions.
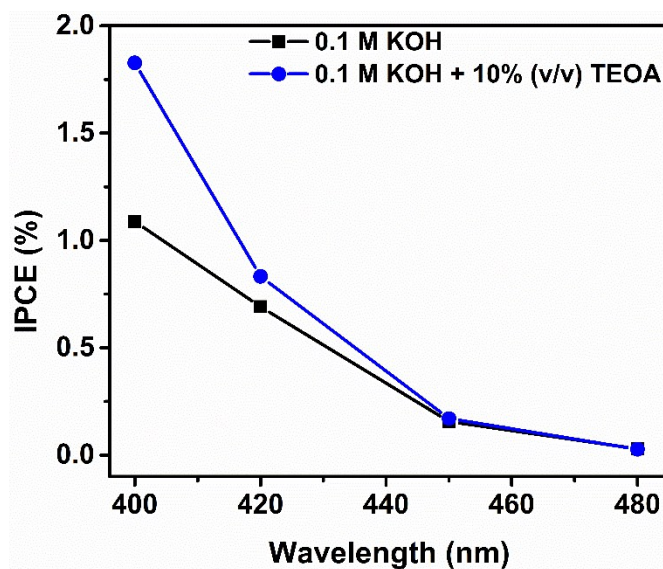
Fig. S20 IPCE measurements of CN-CM$_{120}$M electrode in 0.1 M KOH aqueous solution with and without 10% v/v TEOA upon 1 sun illumination.
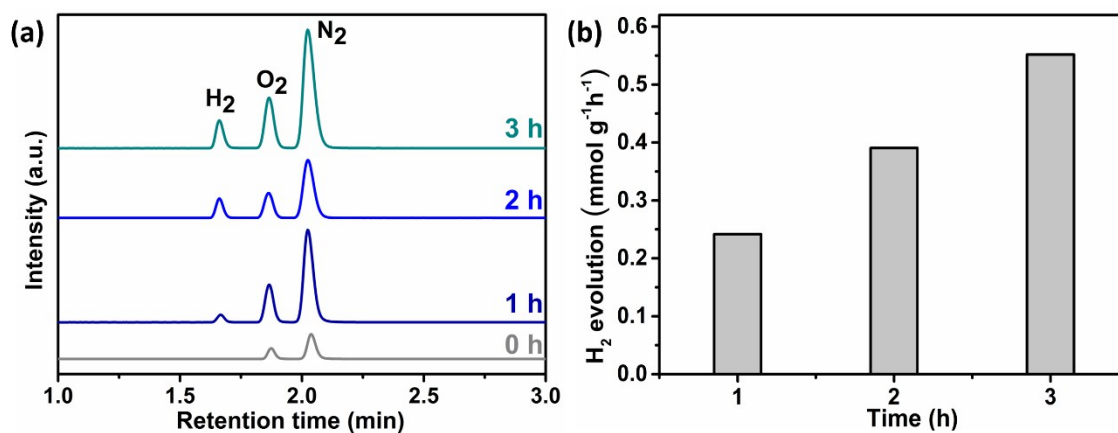

Fig. S21 (a) Gas chromatograph of CN-CM$_{120}$M as the photoelectrocatalyst biased at 1.23 V *vs.* RHE, under constant 1 sun illumination, and (b) H$_2$ production rates of CN-CM$_{120}$M in 0.1 M KOH containing 10% (v/v) TEOA.